Numerical Modelling of Brittle-Ductile Transition with the MUFITS Simulator

Andrey Afanasyev

Institute of Mechanics, Moscow State University

1 Michurinsky Prospekt, Moscow 119192, Russia

E-mail: afanasyev@imec.msu.ru; tel: +74959395767

Abstract

Numerical modelling of flows in geologic porous media with account for plastic behavior of rocks at high temperatures and hydrofracturing at high fluid pressures is required for better understanding of hydrothermal and volcanic systems. Investigation of these systems is limited due to lack of reliable and being at hand reservoir simulation software that accounts for the complicated rock behavior at elevated temperatures. In this paper we present such software as an extension of the MUFITS reservoir simulator. We describe the mathematical model utilized for modelling of elastic and plastic behavior of rocks and input data formats to the simulator. We present several application examples related to modelling of the brittle-ductile transition in hydrothermal systems, in particular perturbed with emplaced degassing magma body, and provide the corresponding simulator input data to facilitate and ease its further usage.

Key words: Porous media, plastic rock, brittle-ductile transition, hydrothermal system, reservoir simulator, MUFITS

1 Introduction

1.1 On the brittle-ductile transition

Fluid transport in hydrothermal and volcanic systems is complicated by high temperatures and pressures that are reached in deep parts of such systems and near degassing magma bodies. The temperatures and pressures can far exceed that in critical point of water at and over which nonlinear fluid properties complicate flows through geologic porous media. Besides fluid properties the transport in high-temperature hydrothermal, especially porphyry, systems is also complicated by plastic rock behavior Fournier (1999); Parisio et al. (2019). The rock material can be assumed elastic (brittle) only at shallow depths where temperature, T, is relatively low, $T < T_b$ (Fig. 1). With increasing depth and temperature, the plastic (ductile) behavior of rocks becomes progressively more relevant in the brittle-ductile transition zone, at $T_b \leq T \leq T_d$, and below this zone the rocks are ductile, at $T > T_d$. The threshold temperatures T_b and T_d depend on rock material but as suggested by Hayba and Ingebritsen (1997); Weis et al. (2012) we assume $T_b = 360°C$ and $T_d = 500°C$.

The transition from brittle to ductile zone results in redistribution of local stresses and strains in the rock matrix what influences fluid transport (Streit and Cox, 2001; Cox, 2010; Weis et al., 2012). In particular, relaxation of the differential stress at high temperatures increases the failure pressure, that is the maximum pore pressure the porous rock can sustain. Also, the permeability of plastic rock matrix reduces at elevated temperatures (Watanabe et al., 2017). As proposed by Weis (2015) for tectonically active Earth crust, the local stress state and permeability of rocks can be characterized by two empirical functions of pressure and temperature. First is the failure pressure given as function of T and being equal to lithostatic pressure at high T. The other function defines the permeability dependence on temperature and fluid pressure. The permeability of rocks is set to decrease with temperature and increase with pressure describing counteraction between plastic permeability closure at high temperatures and its opening at high pressures. Using such parametrization Weis et al. (2012); Weis (2015) simulated formation of a porphyry deposit above degassing magma body also applying a model of hydrofracturing at elevated pressures. It was found that a strong interaction between the permeability changes below the brittle-ductile interface and phase transitions in the fluid can cause permeability waves traveling from magma
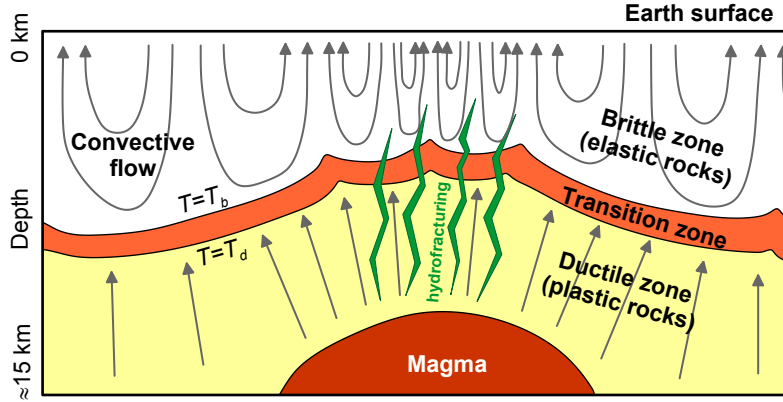
2

Figure 1: Schematic view of the investigated processes that are induces by magma degassing and the hot exsolved fluid flow to surface. The degassing leads to local uplift of the brittle-ductile transition which is limited from above by hydrothermal convection. The flow is complicated by the plastic behavior of rocks and hydraulic fracturing. The gray lines are the instant fluid streamlines.

body to the Earth surface. In these waves the hydraulic fracturing of rocks alternates with the ductile creep what is supported with geologic evidence of multiple episodes of fracturing in porphyry systems (Sillitoe, 2012).

Besides porphyry deposits, modelling of fluid flow in porous rocks with account for transport through the brittle-ductile transition zone has a more general application area to all kinds of hydrothermal systems which can be saturated with different and more complicated multicomponent fluids, as compared to the NaCl-H_2O mixture considered by Weis (2015), and can include inhomogeneous and anisotropic rock material. Many hydrothermal and volcanic systems exhibit periodic behavior (e.g., Chiodini et al., 2016; Jasim et al., 2018) that can be tried to explain with permeability changes in the brittle-ductile transition zone. Such explanations are limited nowadays due to lack of simulation software capable of modelling of the rock properties in the ductile zone. Indeed, only the fluid transport in elastic rocks can be simulated with the available academic simulators (TOUGH2, Pruess et al. (2012); HYDROTHERM, Hayba and Ingebritsen (1994); Open Porous Media Initiative, Lie et al. (2012); and others) and more advanced industrial reservoir simulators. Their application areas are mostly

related to flows at relatively shallow depths (petroleum reservoirs, subsurface gas storage, geothermal energy extraction, etc.) not covering the temperatures of the ductile zone. The only exception is the CSMP++ software (Geiger et al., 2006; Coumou et al., 2008) that was recently applied by Weis (2015) to the porphyry deposits. However, this software remains not available to scientific community as applicable in "one click" simulator with examples of input data and comprehensive manual.

1.2 Scope of this work

In this work we present an extension of the MUFITS reservoir simulator for the brittle-ductile transition modelling in accordance with the noted parametrization of Weis (2015). The simulator merges the standard for petroleum industry accelerated numerical algorithms and input data formats with a number of complicated fluid property modules that extend its application area to hydrothermal and volcanic systems (Afanasyev, 2015). Previously, the simulator was applied to investigation of fluid flows in kimberlite pipes (Afanasyev et al., 2014), deep supercritical parts of hydrothermal systems (Afanasyev et al., 2015), porphyry systems (Afanasyev et al., 2018), and others. Although each of these applications concerns flows at high temperatures (at $T > T_d$), the plastic behavior of rocks was neglected. Understanding of these flows can be improved by accounting for the dynamic permeability changes in and below the brittle-ductile transition. This work aims at presenting the MUFITS extension which provides necessary software developments for further application by scientific community to the noted and other geophysical systems.

Because the present paper concerns the development of the new modelling option and not its application to a particular geophysical system, we keep the fluid as simple as possible. We assume that rocks are saturated with pure H_2O in single-phase liquid (or supercritical fluid) state. Thus, investigation of the permeability waves (Weis, 2015) which are partly induced by phase transitions in the NaCl-H_2O fluid lies outside the scope of this work. We give more attention to possible simulation scenarios and boundary conditions by presenting simple problem statements that can further be used as templates for development of more complicated numerical reservoir models. The problem statements are new because they are designed for demonstration and validation of simulator applicability to modelling of the brittle-ductile transition rather than

4

⁹⁸ the multiphase flows in elastic rocks that were considered by Hayba and Ingebritsen
⁹⁹ (1997); Pruess et al. (2012); Weis et al. (2014), and others. Previously, MUFITS was
¹⁰⁰ extensively validated against such "multiphase" benchmark problems (e.g., Afanasyev,
¹⁰¹ 2015; Afanasyev et al., 2016), therefore we do not consider them here assuming that
¹⁰² the simulator accuracy for modelling fluid transport is proven.

¹⁰³ The application examples, besides demonstration of the software capabilities, have
¹⁰⁴ also a scientific value as byproduct because they uncover the influence of hydrothermal
¹⁰⁵ convection in the shallow brittle zone on depth of the brittle-ductile transition.

¹⁰⁶ 2 Mathematical model

¹⁰⁷ 2.1 Basic equations

For simplicity, we formulate the model for non-isothermal flow of a single-phase fluid
assumed to be H_2O in further application examples presented in Sect. 4. Such flow in
a porous medium is governed by the equations (e.g., Aziz and Settari, 1979; Pruess et
al., 2012; Afanasyev, 2013)

$$\partial_t \left(\phi \rho \right) + \nabla \left(\rho \mathbf{w} \right) = 0 \tag{2.1}$$

$$\partial_t \left(\phi \rho e + (1 - \phi) \rho_r e_r \right) + \nabla \left(\rho h \mathbf{w} - \lambda \nabla T \right) = 0 \tag{2.2}$$

$$\mathbf{w} = -\frac{\mathbf{K}}{\mu} \left(\nabla P - \rho \mathbf{g} \right) \tag{2.3}$$

$$\rho(P, T), \quad h(P, T), \quad \mu(P, T) \tag{2.4}$$

$$\rho_r = const, \quad e_r = C_r T, \quad \lambda = const \tag{2.5}$$

¹⁰⁸ where $\partial_t = \partial / \partial t$, ϕ is the porosity, ρ is the fluid density, $\mathbf{w}$ is the Darcy's velocity, e
¹⁰⁹ is the specific internal energy, ρ_r, e_r and C_r are the rock density, internal energy and
¹¹⁰ heat capacity, $h = e + P/\rho$ is the fluid enthalpy, λ is the heat conductivity of saturated
¹¹¹ porous medium, T is the temperature, $\mathbf{K}$ is the permeability tensor, μ is the viscosity,
¹¹² P is the fluid pressure, and $\mathbf{g}$ is the gravity acceleration.

¹¹³ Eq. (2.1) is the mass conservation equation for the fluid. Eq. (2.2) is the energy
¹¹⁴ conservation equation for saturated porous medium in that we account for both the
¹¹⁵ convective and conductive heat transfer (the terms $\rho h \mathbf{w}$ and $-\lambda \nabla T$, respectively).
¹¹⁶ Eq. (2.3) is the Darcy's law. The functions (2.4), which are assumed to be given, are

the equations of state for fluid. The relations (2.5) define the thermophysical parameters of rock, where for simplicity we assume that rock material is incompressible and its heat conductivity and capacity are constant.

We assume that the permeability tensor (e.g., Aziz and Settari, 1979; Fanchi, 2006)

$$\mathbf{K} = \begin{pmatrix} K_{xx} & K_{xy} & K_{xz} \\ K_{xy} & K_{yy} & K_{yz} \\ K_{xz} & K_{yz} & K_{zz} \end{pmatrix} \qquad (2.6)$$

is the sum of two terms

$$\mathbf{K} = \mathbf{K}_d + \mathbf{K}_s \qquad (2.7)$$

where $\mathbf{K}_d$ is the permeability of dynamic fractures that can open only at high pressures and $\mathbf{K}_s$ is the permeability of matrix, i.e. the medium between fractures. The matrix permeability remains constant (static) in the brittle zone and reduces with temperature in the ductile zone (Watanabe et al., 2017). Hence, according to Eq. (2.7), we follow the single-medium approach for the dynamic fractures modelling that assumes modification of the hydraulic conductivities in elementary volumes of the medium through which fractures pass (e.g., van Lingen et al., 2001).

2.2 Equations for the dynamic fractures

The fractures permeability is described with the following relationship

$$\mathbf{K}_d = \mathbf{K}_{d,\mathrm{max}}\xi \qquad (2.8)$$

where $\mathbf{K}_{d,\mathrm{max}}$ is the tensor of maximum permeability, i.e. at maximum aperture of fractures, and the empirical parameter ξ characterizes the aperture. The values of $\xi = 0$ and $\xi = 1$ correspond to fully closed and opened fractures, respectively, whereas $0 < \xi < 1$ correspond to partly opened fractures.

The progressive hydrofracturing, that is the incremental opening of dynamic fractures if the fluid pressure exceeds the local stress state-dependent failure criterion, is governed by the following equations

$$\partial_t \xi_0 = F(\lambda), \quad \xi = \min\left(\xi_{\mathrm{max}}(\lambda), \max\left(0, \xi_0\right)\right) \qquad (2.9)$$

where $F(\lambda)$ and $\xi_{\mathrm{max}}(\lambda)$ are given functions and

$$\lambda = \frac{P}{P_*}$$

6

is the pore-fluid factor, i.e. the fluid pressure P over the rock failure pressure $P_* = P_{fail}$ (Streit and Cox, 2001; Cox, 2010). The failure pressure P_{fail} is the fluid pressure at which a critical stress for brittle rocks is reached, then leading to hydrofracturing. The non-decreasing functions $\xi_{\max}(\lambda)$ and $F(\lambda)$ define for every given λ the maximum aperture and the rate at which the fractures close or open. They are assumed to satisfy the following constraints

$$F(1) = 0, \qquad \forall \lambda : \quad \frac{dF}{d\lambda} \geq 0, \quad \frac{d\xi_{\max}}{d\lambda} \geq 0 \qquad (2.10)$$

The function $F(\lambda)$ is equal to 0 if $\lambda = 1$ (Fig. 2). Therefore, according to Eqs. (2.8)–(2.10), if $\lambda < 1$ then the aperture ξ decreases with time ($\partial_t \xi_0 \leq 0$) what corresponds to reduction of the permeability $\mathbf{K}_d$ due to fractures closing. On the other hand if $\lambda > 1$ (i.e. if P is high) then ξ increases with time ($\partial_t \xi_0 \geq 0$) what corresponds to production of the permeability $\mathbf{K}_d$ due to fractures opening.

Using a particular shape of function $F(\lambda)$ one can specify either the reversible hydrofracturing when fractures close with pressure decrease or the irreversible hydrofracturing when once created fractures are not closing. In the case of reversible behavior the function $F(\lambda)$ has intervals of both positive values at $\lambda > 1$ and negative values at $\lambda < 1$ (Fig.2, line 1). Thus, if in an elementary volume of porous medium the fluid is released through a fracture then λ (and P) drop down and, according to Eq. (2.9), the fracture permeability reduces. In the case of irreversible behavior the function $F(\lambda)$ is non-negative both at $\lambda \geq 1$ and within an interval at $\lambda < 1$ (Fig. 2, line 2) leading to the non-negative derivative $\partial_t \xi_0$ what means that fractures are not closing.

Our Eq. (2.9) differs from Eq. (14) in Weis (2015) in that it does not depend on the time step of numerical algorithm. Furthermore, according to Eq. (2.9), the fractures close progressively with time when the fluid pressure is released ($\lambda < 1$) whereas instant fractures closing at $\lambda < 1$ is assumed in Weis (2015). It should be noted that a more standard approach for the dynamic fractures modelling is based on the following, instead of Eq. (2.9), relationship for ξ_0 (e.g., Pedroso and Correa, 1997):

$$\xi_0 = \exp\left(\gamma \left(P - P_{fail}\right)\right) \qquad (2.11)$$

where γ is a positive constant. However in the present study aimed at the brittle-ductile transition modelling we use Eq. (2.9) to be consistent with Eq. (14) in Weis (2015). In other studies the hydraulic fracturing can be described with the relation (2.11) by
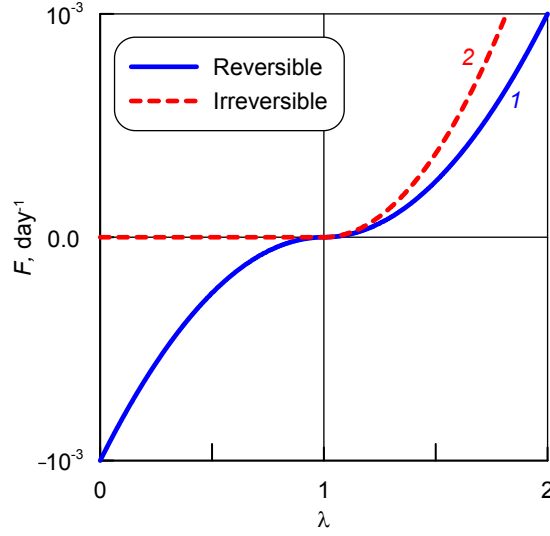
7

Figure 2: Examples of the function $F(\lambda)$ for reversible and irreversible hydrofracturing, lines 1 and 2, respectively.

setting $\xi_{\max}$ equal to the right-hand-side of Eq. (2.11) and specifying large positive values of F for $\lambda > 1$. According to Eq. (2.9), in this case ξ_0 will be equal to $\xi_{\max}$ due to the high permeability production rate F. Thus, our model of dynamic fractures merges the standard approach with Eq. (14) in Weis (2015).

The tensor $\mathbf{K}_{d,\max}$ characterizes local directions of fractures. For example, in the case of a system of horizontal fractures one can specify zero xz, yz and zz and non-zero xx, xy and yy components of the tensor $\mathbf{K}_{d,\max}$ (see Eq. 2.6).

2.3   Equations for the plastic rock permeability

For modelling the ductile closure of permeability and its counteracting opening at elevated pressures we follow the formulation proposed by Weis (2015) which implies that for every radius-vector $\mathbf{r}$ the permeability of plastic rocks depends on λ and T whereas the failure pressure is the function of only T:

$$\mathbf{K}_s(\lambda, T) = \mathbf{K}_{s,\max} D(\lambda, T), \qquad P_*(T) = P_{fail} + (P_{lith} - P_{fail})\, \eta(T) \qquad (2.12)$$

Here, $\mathbf{K}_{s,\max}$ is the maximum permeability, i.e. if rocks are elastic at low $T < T_b$ in the brittle zone, P_{lith} can be interpreted as the lithostatic (or overburden) pressure, and
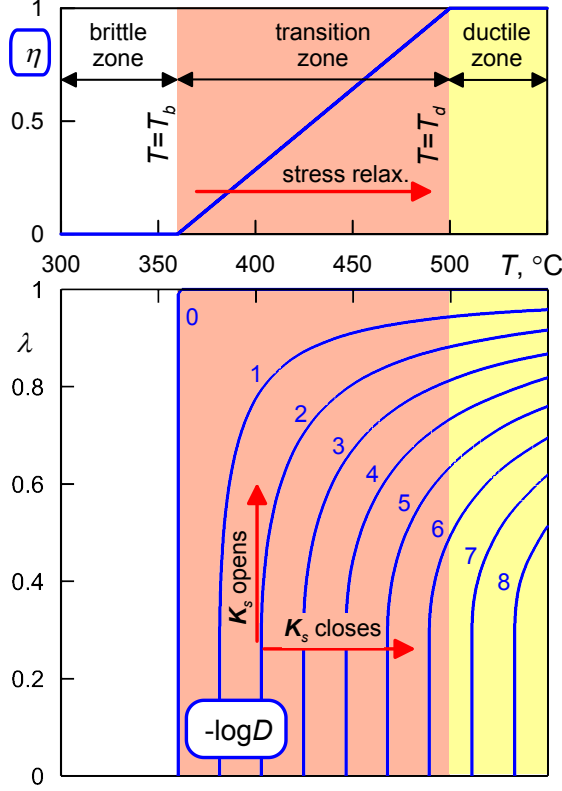
Figure 3: Example of the functions $\eta(T)$ and $D(\lambda, T)$ for the plastic rock model.

$D(\lambda, T)$ and $\eta(T)$ are given function of the form schematically shown in Fig. 3, where, as before, the temperature intervals $T < T_b$, $T_b \leq T \leq T_d$ and $T > T_d$ correspond to the brittle, transition and ductile regions, respectively (Fig. 1).

The functions D and η characterize the plastic behavior of rock material. The following constraints for $D(\lambda, T)$ and $\eta(T)$ hold

$$\forall \lambda, T: \quad D(\lambda, T_b) = 1, \quad D(1, T) = 1, \quad \frac{\partial D}{\partial \lambda} \geq 0, \quad \frac{\partial D}{\partial T} \leq 0, \quad \frac{d\eta}{dT} \geq 0$$

$$\forall T < T_b: \quad \eta(T) = 0, \quad D(\lambda, T) = 1 \quad \forall T > T_d: \quad \eta(T) = 1$$

(2.13)

According to Eq. (2.13) the permeability is constant in the brittle zone, $\mathbf{K}_s = \mathbf{K}_{s,\max}$, because $D \equiv 1$ at $T < T_b$, and the function $\eta(T)$ is equal to 0 what leads to $P_* = P_{fail}$. In the transition zone $T_b \leq T \leq T_d$ the failure pressure P_* increases to the overburden pressure P_{lith} with rising T. This can be interpreted as a result of the differential stress relaxation at high temperature (Fournier, 1999; Cox, 2010). In the ductile zone $T > T_d$

9

the failure pressure is equal to the lithostatic pressure $P_* = P_{lith}$ ($\eta = 1$). With a fixed λ (i.e. fixed P) and increasing $T > T_b$, the permeability decreases over several orders of magnitude modelling the ductile creep of hot rocks ($\partial D / \partial T \leq 0$; Fig. 3). This permeability closing is counteracted by its opening with rising λ ($\partial D / \partial \lambda \geq 0$). Indeed, for a fixed $T > T_b$ and rising λ the function D increases reaching $D = 1$ at $\lambda = 1$.

2.4 Parametrization in space

The models of hydraulic fracturing and ductile creep are parametrized in space with the following distributions

$$P_{fail}(\mathbf{r}), \quad P_{lith}(\mathbf{r}), \quad \mathbf{K}_{d,\max}(\mathbf{r}), \quad \mathbf{K}_{s,\max}(\mathbf{r}) \tag{2.14}$$

where $\mathbf{r}$ is the radius-vector. Before the fluid flow modelling, the distributions of strains and stresses of rocks can be calculated with account for its fractures and faults network and forces applied to considered geologic reservoir, e.g. tectonic extension or compression or volcanic edifice load (Parisio et al., 2019). From that calculation the distributions (2.14) can be derived and then used in the dynamic modelling of fluid flow. For instance the distributions (2.14) can be specified using the averaged depth-dependent relationships for tectonically active crust. The permeability $\mathbf{K}_{s,\max}$ can follow the logarithmic profile of Manning and Ingebritsen (1999) whereas the overburden pressure P_{lith} can linearly increase with depth. The failure pressure P_{fail} can also be specified as a function of depth being the maximum pore pressure of the brittle shear and extension (Weis, 2015).

A more comprehensive approach, which although lies outside the scope of the present work, could be a full hydro-mechanical coupling when the distributions (2.14) are modified dynamically by calculation at every time the stress state in the reservoir. In practice, this can be implemented through a program interface between hydrodynamic and geomechanic simulators.

3 Numerical implementation

The models described in Sect. 2.2 and 2.3 are implemented in MUFITS as two separate modelling options. The first option allows the dynamic fractures modelling in

accordance with the equations in Sect. 2.2 whereas the second option extends MUFITS for the plastic behavior of rocks modelling as it is described in Sect. 2.3. The model parameters, in particular the empirical functions $F(\lambda)$, $\eta(T)$ and $D(\lambda, T)$ characterizing the rock material properties, can be specified in an engineering manner using tabulated input format which is described in Appendix.

The principal directions of the static and dynamic permeability tensors, $\mathbf{K}_{s,\mathrm{max}}$ and $\mathbf{K}_{d,\mathrm{max}}$, are assumed to be aligned with the grid. Therefore, the mixed components of the tensors (xy, yz and xz, see Eq. (2.6)) are equal to zero.

The standard for reservoir simulation fully-implicit method is applied in the examples presented in Sect. 4. The finite volume approach with the upwind discretization scheme is utilized (Aziz and Settari, 1979; Fanchi, 2006). The primary simulation variables are the pressure, P, and the temperature, T.

Both modelling options can be applied with any non-isothermal equation of state module implemented in MUFITS (Afanasyev, 2015).

4 Example simulations

4.1 Overview

In order to demonstrate the models application with MUFITS we consider several 1D and 2D benchmark simulation scenarios. The problem set-up is schematically shown in Fig. 4. We apply homogeneous Cartesian griding to the rectangular domain of 36 km width and 12 km height which corresponds to a cross-section of the Earth crust. Thus the porosity and matrix permeability follow the average depth-dependent profiles for tectonically active continental crust (Vitovtova et al., 2014; Manning and Ingebritsen, 1999):

$$\log \phi = -0.65 - 0.1z + 0.0019z^2$$

$$\log K_{s,\mathrm{max}} = 1 - 3.2 \log z, \qquad K_{s,\mathrm{max}} = (K_{s,\mathrm{max}})_{xx} = (K_{s,\mathrm{max}})_{zz}$$

where and in what follows z units are km, the permeability units are mD (millidarcy), and the pressure units are bar. The maximum fractures permeability is assumed to be five times the matrix permeability

$$K_{d,\mathrm{max}} = 5K_{s,\mathrm{max}}, \qquad K_{d,\mathrm{max}} = (K_{d,\mathrm{max}})_{xx} = (K_{d,\mathrm{max}})_{zz}$$
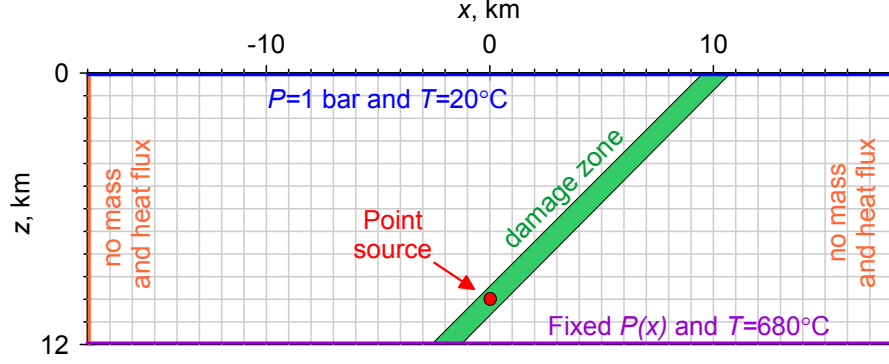
11

Figure 4: The simulation domain. The point source is specified only in the problems 3a and 3b. The damage zone is used only in problem 3b.

The failure and lithostatic pressures follow the depth-dependent linear profiles:

$$P_{fail} = 1 + 100z, \qquad P_{lith} = 1 + 270z \tag{4.1}$$

The function $F(\lambda)$ for dynamic permeability model is a quadratic function (Weis, 2015):

$$F(\lambda) = 0.001(\lambda - 1)^2 \tag{4.2}$$

where F units are 1/day. The function's (4.2) graph is the line 1 in Fig. 2.

The failure pressure and the permeability of plastic rock are governed by the relations

$$T < T_b: \quad \eta = 0, \qquad T \in [T_b, T_d]: \quad \eta(T) = \frac{T - T_b}{T_d - T_b}, \qquad T > T_d: \quad \eta = 1$$

$$\lambda \geq \lambda_{\min}: \quad D(\lambda, T) = a\left(1 - \left(\frac{\lambda - \lambda_{\min}}{1 - \lambda_{\min}}\right)^2\right) \tag{4.3}$$

$$\lambda < \lambda_{\min}: \quad D(\lambda, T) = D(\lambda_{\min}, T)$$

where the constants $T_b = 360°C$, $T_d = 500°C$, $a = 6.5$, and $\lambda_{\min} = 0.3$ are chosen to resemble parameters of the Weis (2015) model. The constraints (2.13) are hold for the functions (4.3) plotted in Fig. 3.

Other rock parameters are $\rho_r = 2700$ kg/m^3, $C_r = 1$ kJ/(kg°C), and $\lambda = 2$ W/(m°C).

The fluid is assumed to be pure H_2O. The functions (2.4) are calculated using cubic equation of state for water (Afanasyev, 2013) calibrated against IAPWS formulation for the H_2O properties. The initial and boundary conditions for the problems considered below are intentionally chosen to avoid H_2O partitioning in vapor and liquid phases. Thereby, we reduce the problem complexity because the phase transitions can lead to periodic behavior of flows (McGuinness et al., 1993; Weis, 2015). Thus H_2O remains in single-phase state of liquid or supercritical fluid at high P and T.

At the initial moment of time, $t = 0$, we specify that the pressure is equal to the lithostatic pressure and the temperature is a linear function of depth corresponding to the geothermic gradient of 55°C/km:

$$t = 0: \quad P = P_{lith}, \quad T = 20 + 55z \qquad (4.4)$$

We impose the atmospheric pressure and temperature at the open top boundary $z = 0$ km, corresponding to the the Earth surface, and also keep constant P and T at the bottom boundary $z = 12$ km:

$$z = 0 \text{ km:} \quad P = 1, \quad T = 20°C \qquad (4.5)$$

$$z = 12 \text{ km:} \quad P = P_{lith} - \Delta P(x), \quad T = 680°C \qquad (4.6)$$

The P and T values in conditions (4.5) and (4.6) are in accordance with the depth-dependent profiles (4.1) and (4.4). The left and right boundaries, $x = \pm 18$ km, are impermeable and heat insulated. They do not influence the processes in the center part of the domain at $x = 0$ km.

4.2 Benchmark problem 1

First we consider the 1D problem when the Cartesian grid has only one element along axis x. The pressure at $z = 12$ km is kept $\Delta P = 75$ bar less than the lithostatic pressure (see Eq. (4.6)). According to Eqs. (4.1) and (4.6) it is equal to 3186 bar.

At $t > 0$ the pressure and temperature redistribute in the domain during initial transient processes and the steady state distribution evolves at $t \geq 250$ ky (Fig. 5). In this steady state the pressure follows hydrostatic distribution in the shallow part of the domain $z < 4.5$ km, where $T < T_b$. Here, the pressure gradient $\nabla_z P$ decreases with depth, z, leading to a nonlinear distribution $P(z)$ which is caused by the fluid density
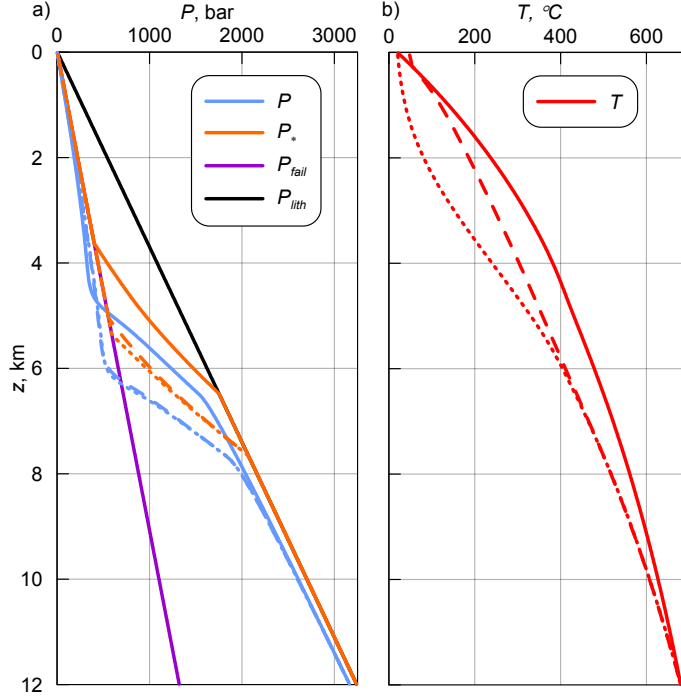
13

Figure 5: Distributions of P and T at $t = 500$ ky in problem 1 (solid lines) and problem 2 along an ascending and descending plume (dashed and dotted lines).

decrease with rising T. In the bottom part of the system at $z > 6.5$ km ($T > T_d$) the pressure has approximately equal difference ΔP from the lithostatic pressure as at the bottom boundary and in general it follow the linear lithostatic profile. The depth interval of $z \in [3.5, 6.5]$ km corresponds to the brittle-ductile transition where P changes with depth from the hydrostatic to the lithostatic value.

The pressure is less than the failure pressure P_* over the whole depth interval, thus the hydrofracturing does not occur ($\xi = 0$).

The distribution of T differs from the initial linear profile; the $T(z)$ graph is a convex upward curve (Fig. 5b). This is because the imposed boundary condition (4.6) for P results in a small H_2O flux from bottom to top of the domain of 0.0069 kg/(day·m^2) magnitude. Indeed, this is caused by a larger than the hydrostatic value of pressure. The flux magnitude is controlled by the pressure difference from the lithostatic pressure, ΔP, at $z = 12$ km. A smaller ΔP leads to a larger flux. Thus the temperature profile is affected by both the conductive and the convective heat transport and the convective

14

flux results in the convex upward distribution $T(z)$.

4.3   Benchmark problem 2

4.3.1   Problem 2a

The mathematical statement of the problem 2a is identical to that of the problem 1 with the exception of grid resolution. Now, the problem is 2D, i.e. the grid has multiple grid blocks along both x and z axes (Fig. 4). As before, the fixed pressure of 3186 bar and temperature of 680°C are maintained at the bottom boundary, $z = 12$ km (see Eq. (4.6)).

The simulation results are shown in Figs. 5 and 6a at $t = 500$ ky. The temperature remains below T_d in the top ≈ 5.5 km of the domain corresponding to the brittle zone. Here, the convective flow develops in which the plumes of hot ascending fluid alternate with the plumes of colder descending fluid. The fluid cools down near the top boundary, corresponding to the Earth surface, then it sinks down to the brittle-ductile transition. Near the transition zone the fluid heats up and expands and then due to buoyancy it ascends back to surface. Thus, the convection is limited from below by the brittle-ductile transition, located at $z \in [5, 8]$ km. The flow at $t = 500$ ky (Fig. 6) occurs under quasi-steady state what means that the plumes are not actually steady. They move laterally along axis x, and two plumes can merge at some times what is followed by formation of a new plume. However, the average distance between the plumes remains constant. In the transition and ductile zones ($z > 6$ km) the convection does not develop. Here the flow is in direction from bottom to top.

The pressure and temperature along vertical straights passing through an ascending ($x = 0.3$ km) and descending ($x = -2.5$ km) plume are shown in Fig. 5. These temperatures coincide in the ductile zone whereas in the brittle zone T is higher in the ascending than in the descending plume for every depth z (Fig. 5b).

The convection (problem 2a) moves the brittle-ductile transition 1 km deeper as compared to the 1D case of no convection (problem 1). Indeed as shown in Fig. 5a the pressure changes from hydrostatic to lithostatic value in a 1 km deeper zone. This is caused by that the convection leads to more intense, as compared to the heat conduction, heat transfer to surface. In the case of convection the brittle-ductile transition zone is cooled more intensely and so it moves deeper into hotter region. The convection also
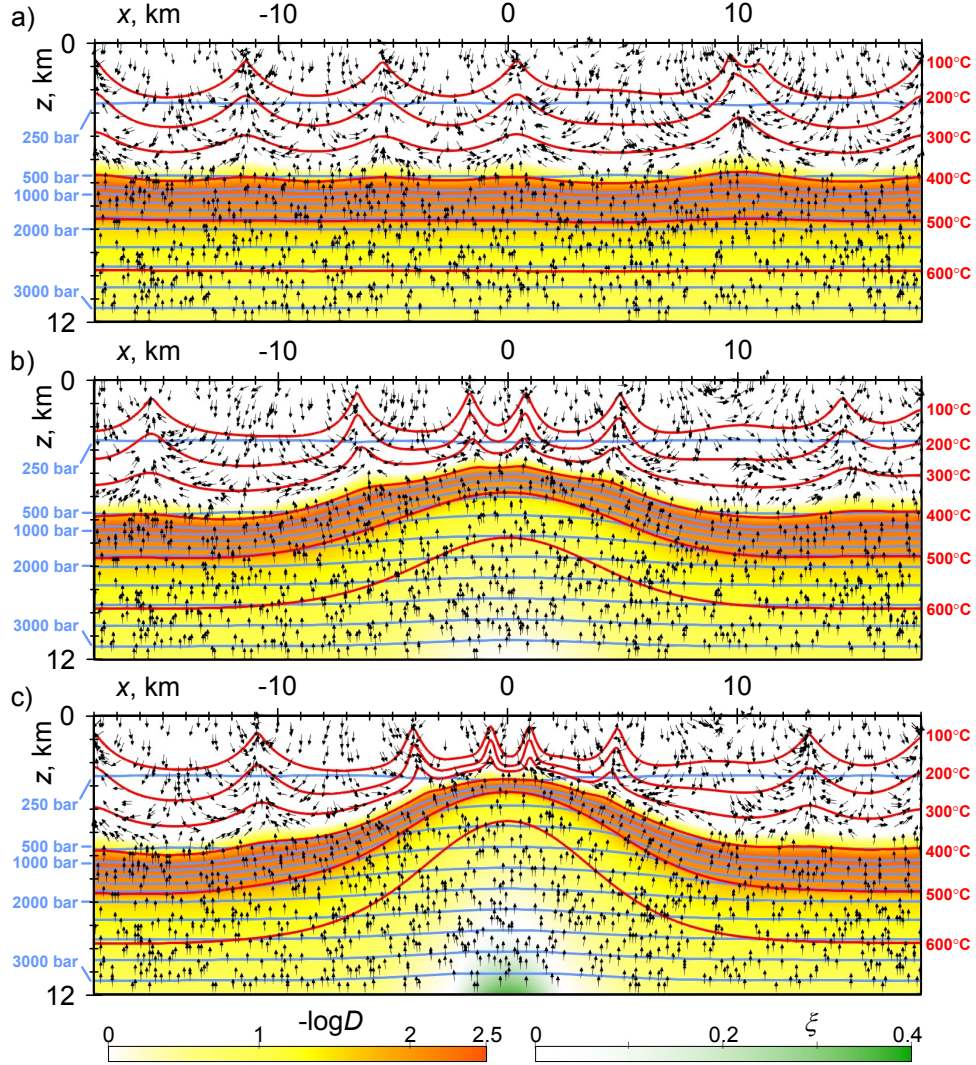
Figure 6: Simulation results at $t = 500$ ky for the problems 2a, 2b and 2c (a, b and c, respectively). The color shows the distribution of $-\log D$ and ξ, the black arrows are direction of the fluid flow, and the blue and red lines are isobars and isotherms, respectively.

increases the temperature gradient in the ductile zone (Fig. 5b) because a larger heat flux through this zone is needed to support convection near the surface. Another effect that can be seen in Fig. 6 is that the ascending plumes locally (beneath them) move the transition zone upward because T is higher in such plumes. This localized uplift shift of the transition follows the plumes when they move laterally in the intermittent convection.

4.3.2   Problem 2b

Now we modify the problem 2 and impose elevated pressure at the bottom boundary $z = 12$ km near $x = 0$ km. Thus we assume that the boundary conditions are (see also Eq. (4.6))

$$z = 12 \text{ km}: \qquad \Delta P = 75 - A \exp\left(-\left(\frac{z}{5}\right)^2\right), \quad T = 680^\circ\text{C} \qquad (4.7)$$

where $A = 75$ bar. The distribution (4.7) is shown in Fig. 7. The higher pressure in the center region near $x \approx 0$ km can be interpreted as the influence of a magma body emplaced at $x = 0$ km and $z > 12$ km. When magma cools down and solidifies the hot fluid is exsolved in the rocks above it what is simulated with elevated pressures imposed at $x \approx 0$ km and $z = 12$ km.

The simulation results for the problem 2b are shown in Figs. 6b and 7. The elevated pressure at the bottom results in a locally higher flux into the domain through the boundary $z = 12$ km (Fig. 7). The flux increases up to 0.049 kg/(m^2·day) at $x = 0$ km leading to upward movement of the transition zone which stabilizes at shallower depth of 4–5.5 km than that near $x = \pm 18$ km. The higher heat flux in the center region intensifies convection leading to more frequent plumes near $x = 0$ km.

The pore pressure P stays below the failure pressure P_{fail} for every $\mathbf{r}$ in the problems 2a and 2b, thus the hydraulic fracturing does not occur ($\xi = 0$).

4.3.3   Problem 2c

Now we increase the pressure "anomaly" at the bottom by setting $A = 100$ bar in the boundary condition (4.7). Consequently, the pressure exceeds the failure (overburden) pressure at $z = 12$ km triggering the hydraulic fracturing.

The simulation results for this problem 2c are shown in Figs. 6c and 7. A higher, as compared to the problem 2b, pressure at $x = 0$ km, $z = 12$ km results in a larger fluid
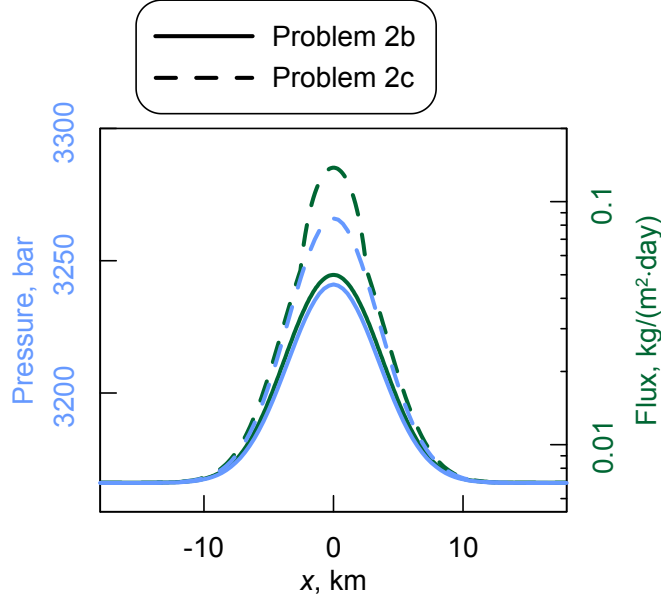
Figure 7: The pressure and the calculated fluid flux at $z = 12$ km.

flux from bottom into the domain which maximum of 0.137 kg/(day·m^2) is reached at $x = 0$ km. The fractures open up to ≈ 8 km depth in order to allow the higher flux ($\xi > 0$ in the bottom of Fig 6c). The transition zone moves up to 2-3 km depth causing very intense convection above it. This upward displacement of the transition results in much narrower ascending plumes and the distance between them reduces from 8 km to 2 km.

4.4 Benchmark problem 3

4.4.1 Problem 3a

The fluid flux from a cooling magma body can also be modelled using a point source. Let us now assume the parameters at the boundary $z = 12$ km are given by Eq. (4.6) where $\Delta P = 75$ bar is constant and the reservoir is perturbed with a point source placed at $x = 0$ km and $z = 10$ km (Fig. 4). A hot fluid of $T = 680°$C at $P = 3000$ bar is injected into the reservoir. The injection begins at $t = 250$ ky and its rate is constant at 1000 kg/(day·m).
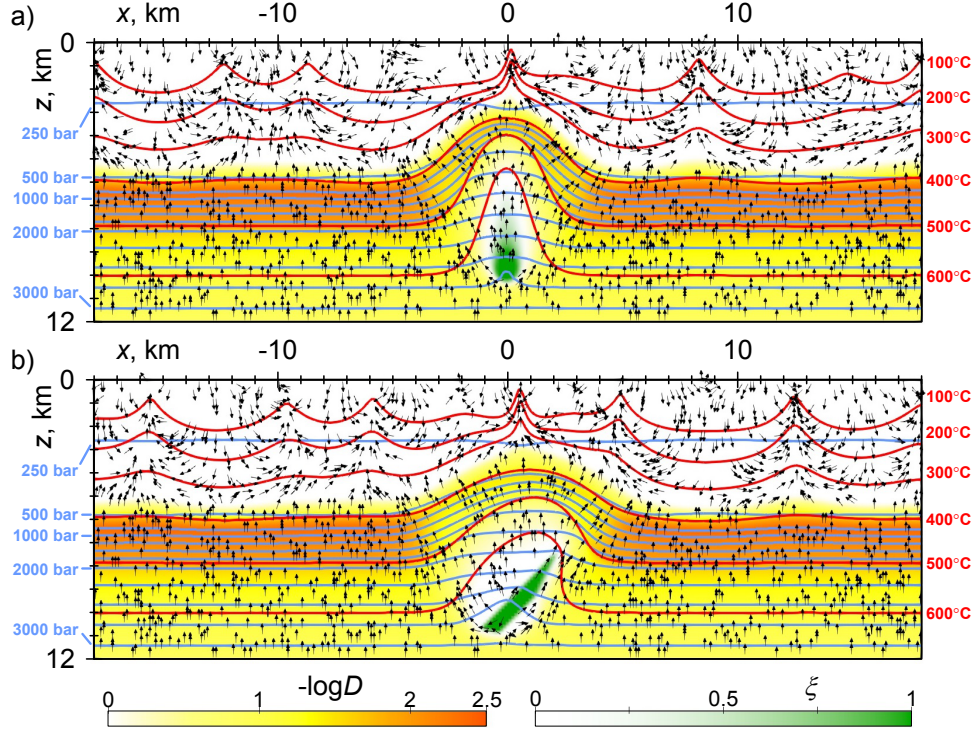
18

Figure 8: Simulation results at $t = 275$ ky for the problems 3a and 3b (a and b respectively). The color shows the distributions of $-\log D$ and ξ, the black arrows are direction of the fluid flow, and the blue and red lines are isobars and isotherms.

The simulation results are shown in Fig. 8a at $t = 275$ ky. The fluid injection triggers hydrofracturing near the point source and above it. A high-permeability pathway forms through which the fluid flows through the ductile and transition zones reaching the region of convection in the brittle zone. Thereby, the transition zone moves upward above the point source.

4.4.2 Problem 3b

The scenario 3b is complicated by imposing an inclined damage zone of 0.5 km width as it is shown in Fig. 4. The angle of inclination is 45°. The hydraulic fracturing is enabled only in the damage zone. This is simulated using two different rock types (i.e. lithological units). The first type is for the damage zone and the second type is for

the rocks outside the damage zone. The hydrofracturing model (Sect. 2.2) is enabled only for the first type of rocks.

The result of the flow simulation over 25 ky of injection is shown in Fig. 8b. The fluid injection causes the fractures opening in the damage zone, and the fluid rapidly ascends to surface through this zone. During initial transient processes the brittle-ductile transition moves up near the damage zone shifting to the right of the point source. Later on after the transient processes ceases the transition shifts back to the center region above the source although the asymmetry partly remains.

5 Summary

The brittle-ductile transition can now be simulated with the MUFITS simulator. The developed modelling options allow simulations of flows in porous media with account for the plastic behavior of rocks at high temperatures and hydrofracturing at elevated pressures. We provide several benchmark examples demonstrating the software applicability and possible boundary conditions. The examples can further be used as templates for more complicated reservoir models development and for benchmarking in other software development efforts. Also, the examples demonstrate that the hydrothermal convection in the shallow brittle zone can significantly change the depth of the brittle-ductile transition. The simulator with the noted development can further be used by scientific community in a more detailed modelling of different transport phenomena in high-temperature hydrothermal and volcanic systems.

Supplementary materials

The presented examples are supplemented with animated figures showing the flow parameters evolution with time. The input data files with comprehensive comments for selected benchmark examples as well as the latest version of the MUFITS executable and its manual can be found at the simulator website www.mufits.imec.msu.ru.

Acknowledgements

Appendix. MUFITS keyword and mnemonics

In this appendix we provide technical aspects of modelling the brittle-ductile transition with the MUFITS simulator. Any input data file to the simulator contains description of the problem in the language of keywords and mnemonics. A keyword is command to the simulator with that a particular modelling option is activated or input data are loaded in simulation. A mnemonic is brief abbreviation of a physical property (e.g., the pressure is PRES). Thus, description of any new modelling option reduces to the description of the corresponding keywords and mnemonics.

The dynamic fractures modelling option based on the equations in Sect. 2.2 is activated by specifying the DYNFRACK keyword in the first configuration section of the input data file. Then the rock failure pressure P_{fail} and the fractures permeability $\mathbf{K}_{d,\max}$ must be specified for every grid blocks in the GRID section of the input file. Thereby, the space distributions $P_{fail}(\mathbf{r})$ and $\mathbf{K}_{d,\max}(\mathbf{r})$ are uploaded in the simulation (see Eq. (2.14)). The specification of P_{fail} and $\mathbf{K}_{d,\max}$ is done using standard methods for operations with arrays in MUFITS. The associated mnemonics are given in Table 1. This table also contains the mnemonics for the fractures aperture ξ and the pore-fluid factor λ for reporting calculated distributions of these parameters at selected simulation times.

The functions $F(\lambda)$ and $\xi_{\max}(\lambda)$ in Eq. (2.9) are specified for every rock type by the DYNFRTAB keyword (within the ROCK-ENDROCK brackets) which is followed with a table of the syntax given in Table 2. Thus, the number of DYNFRTAB tables loaded in a reservoir simulation is equal to the number of rock types (or lithological units) present in that reservoir model. The table consists of three column which from left to right correspond to λ, F and $\xi_{\max}$. Every row of the table defines points belonging to the curves $F(\lambda)$ and $\xi_{\max}(\lambda)$. The values of λ in the first column must increase down the table and include the value $\lambda = 1$. Therefore, according to Eq. (2.10), the data in the 2nd and 3rd columns must not decrease down the table and in the row $\lambda = 1$ the

Table 1: MUFITS mnemonics associated with the DYNFRACK and DUCTILE options.

Parameter	Mnemonic
P_{fail}	PRESFAIL
P_{lith}	PRESLITH
P_*	PRESFDYN
$\mathbf{K}_{s,\max}$	PERMX, PERMY, and PERMZ
	(xx, yy, and zz components)
$\mathbf{K}_{d,\max}$	PERMXFR, PERMYFR, and PERMZFR
	(xx, yy, and zz components)
D	DCTTMULT
ξ	TRANFRMT
λ	PFLDFACT

Table 2: The DYNFRTAB keyword syntax

DYNFRTAB

λ_1	F_1	$(\xi_{\max})_1$	/
λ_2	F_2	$(\xi_{\max})_2$	/
$\vdots$	$\vdots$	$\vdots$	/
λ_m	F_m	$(\xi_{\max})_m$	/
/			

function F in the second column must be equal to 0. The default value of $\xi_{\max}$ in the 3rd column is 1.

The modelling option for the plastic behavior of rocks based on the equations in Sect. 2.3 is activated by specifying the DUCTILE keyword in the first configuration section of the input data file. Then the lithostatic and failure pressures, P_{lith} and P_{fail}, as well as the matrix permeability, $\mathbf{K}_{s,\max}$, must be specified for every grid block in the GRID section of the input file. Thereby, the space distributions $P_{lith}(\mathbf{r})$, $P_{fail}(\mathbf{r})$ and $\mathbf{K}_{s,\max}(\mathbf{r})$ are loaded in the simulation (see Eq. (2.14)). The specification of P_{lith}, P_{fail} and $\mathbf{K}_{s,\max}$ is done using standard methods for operations with arrays in MUFITS. The associated mnemonics are given in Table 1, so the matrix permeability is the "standard" permeability provided for every grid block in any simulation. The Table 1 also contains the mnemonics for the magnitude of ductile creep, $-\log D$, the failure pressure, P_*,

Table 3: The DUCTTAB keyword syntax					
DUCTTAB					
Units	T_1	T_2	$\cdots$	T_n	/
	η_1	η_2	$\cdots$	η_n	/
λ_1	$-\log D_{11}$	$-\log D_{12}$	$\cdots$	$-\log D_{1n}$	/
λ_2	$-\log D_{21}$	$-\log D_{22}$	$\cdots$	$-\log D_{2n}$	/
$\vdots$	$\vdots$	$\vdots$	$\ddots$	$\vdots$	/
λ_k	$-\log D_{k1}$	$-\log D_{k2}$	$\cdots$	$-\log D_{kn}$	/
/					

and the pore-fluid factor, λ, for reporting calculated distributions of these parameters at selected simulation times.

The functions $\eta(T)$ and $D(\lambda, T)$ in Eq. (2.12) are specified for every rock type by the DUCTTAB keyword (within the ROCK-ENDROCK brackets) which is followed with a table of the syntax given in Table 3 (this syntax corresponds to the $\eta(T)$ and $D(\lambda, T)$ graphs layout in Fig. 3). Thus, the number of DUCTTAB tables loaded in a reservoir simulation is equal to the number of rock types (or lithological units) present in that reservoir model. The table consists of arbitrary number of columns and rows which are further denoted as $n + 1$ and $k + 2$ ($n, k \geq 2$).

The data in the first row define the temperatures for which the values of η and D are provided. The first item in the row "Units" defines the units of the following n values of temperature. The possible input values for "Units" are "K" (default value) and "C" corresponding to degrees Kelvin and Celsius respectively. The values of temperature must increase in the row.

The data in the 2nd row define the values of η for the corresponding values of T. According to the constraints (2.13) the values of η are subject to the following rules

- The values of η must not decrease in the row;

- At least one value of $\eta = 0$ and one value of $\eta = 1$ must be present;

- The temperature T_b is the maximum temperature in the 1st row for which $\eta = 0$;

- The temperature T_d is the minimum temperature in the 1st row for which $\eta = 1$.

23

The following rows from 3rd to $k+2$ th are intended for loading the function $D(\lambda, T)$. Here, in every row the first item is λ which is followed with n values of $-\log D$ for this λ and the temperatures defined in the 1st row. The values of λ must decrease down the table and the maximum λ (i.e. λ_1) must be equal to 1. According to the constraints (2.13) the values of D in the table are subject to the following rules:

- The values of $-\log D$ for all $T \leq T_b$ must be equal to 0;

- The values of $-\log D$ for $\lambda = 1$ (i.e. in the 3rd row) must be equal to 0;

- The values of $-\log D$ must not decrease in every row and column.

The cubic and bicubic interpolation is applied to the data provided with the DYN-FRTAB and DUCTTAB keywords in order to calculate $F(\lambda)$, $\xi_{\max}(\lambda)$, $\eta(T)$ and $D(\lambda, T)$ at all intermediate values of λ and T.

The description of other keywords and mnemonics associated to the developed modelling options can be found in the simulator manual at its website www.mufits.imec.msu.ru.

References

Afanasyev, A.A., 2013. Multiphase compositional modelling of CO_2 injection under subcritical conditions: The impact of dissolution and phase transitions between liquid and gaseous CO_2 on reservoir temperature // Int. J. Greenhouse Gas Control. 19: 731–742. DOI: 10.1016/j.ijggc.2013.01.042.

Afanasyev, A., Melnik, O., Poritt, L., Schumacher, J., and Sparks, S.J., 2014. Hydrothermal alteration of kimberlite by convective flows of external water. Contributions to Mineralogy and Petrology. 168:1038. DOI: 10.1007/s00410-014-1038-y.

Afanasyev, A.A., 2015. Hydrodynamic modelling of petroleum reservoirs using simulator MUFITS. Energy Procedia. 76: 427–435. DOI: 10.1016/j.egypro.2015.07.861.

Afanasyev, A., Costa, A., and Chiodini G., 2015. Investigation of hydrothermal activity at Campi Flegrei caldera using 3D numerical simulations: extension to high temperature processes. J. Volcanology Geothermal Res. 299: 68–77. DOI: 10.1016/j.jvolgeores.2015.04.004.

Afanasyev, A., Kempka, T., Kühn, M., and Melnik, O., 2016. Validation of the MUFITS reservoir simulator against standard CO_2 storage benchmarks and history-matched models of the Ketzin pilot site. Energy Procedia. 97: 395–402. DOI:10.1016/j.egypro.2016.10.032.

Afanasyev, A., Blundy, J., Melnik, O., and Sparks, S., 2018. Formation of magmatic brine lenses via focused fluid-flow beneath volcanoes. Earth Planet. Sci. Lett. 486: 119–128. DOI: 10.1016/j.epsl.2018.01.013.

Aziz, K., and Settari, A., 1979. Petroleum reservoir simulation. New York: Appl Sci Publ.

Chiodini, G., Paonita , A., Aiuppa, A., et al., 2016. Magmas near the critical degassing pressure drive volcanic unrest towards a critical state. Nat. Comm. 7:13712. DOI: 10.1038/ncomms13712.

Coumou, D., Matthai, S., Geiger, S., and Driesner, T., 2008. A parallel FE-FV scheme to solve fluid flow in complex geologic media. Computers and Geosciences. 34: 1697–1707. DOI: 10.1016/j.cageo.2007.11.010.

Cox, S.F., 2010. The application of failure mode diagrams for exploring the roles of fluid pressure and stress states in controlling styles of fracture-controlled permeability enhancement in faults and shear zones. Geofluids 10: 217–233. DOI: 10.1111/j.1468-8123.2010.00281.x.

Fanchi, J.R., 2006. Principles of applied reservoir simulation. New York: Gulf Prof Publ.

Fournier, R.O., 1999. Hydrothermal processes related to movement of fluid from plastic into brittle rock in the magmatic-epithermal enviroment. Econ. Geol. 94: 1193–1211. DOI: 10.2113/gsecongeo.94.8.1193.

Geiger, S., Driesner, T., Heinrich, C.A., and Matthai, S.K., 2006. Multiphase thermohaline convection in the Earth's crust: I. A new finite element – finite volume solution technique combined with a new equation of state for NaCl-H_2O. Transp. Porous Med. 63: 399–434. DOI: 10.1007/s11242-005-0108-z.

Hayba, D.O., and Ingebritsen, S.E., 1994. The computer model HYDROTHERM, A three-dimensional finite-difference model to simulate ground-water flowand heat transport in the temperature range of 0 to 1,200 C: U.S. Geological Survey Water-Resources Investigations Report 94–4045, 85 p.

Hayba, D.O., and Ingebritsen, S.E., 1997. Multiphase Groundwater flow near cooling plutons. J. Volcanol. Geotherm. Res. 102(B6), 12235–12252. DOI: 10.1029/97JB00552.

Jasim, A., Hemmings, B. Mayer, K., and Scheu, B., 2018. Groundwater flow and volcanic unrest. In: Gottsmann J., Neuberg J., Scheu B. (eds) Volcanic Unrest. Advances in Volcanology. Springer, Cham. DOI: 10.1007/11157_2018_33.

Lie, K.-A., Krogstad, S., Ligaarden, I.S., Natvig, J.R., Nilsen, H.M., and Skaflestad, B., 2012. Open source MATLAB implementation of consistent discretisations on complex grids. Comput. Geosci., 16(2): 297–322. DOI: 10.1007/s10596-011-9244-4.

Manning, C.E. and Ingebritsen, S.E., 1999. Permeability of the continental crust: implications of geothermal data and metamorphic systems. Rev. Geophys. 37: 127–150. DOI: 10.1029/1998RG900002.

McGuinness, M.J., Pruess, K., O'Sullivan, M., and Blakeley, M., 1993. Geothermal Heat Pipe Stability: Solution Selection by Upstreaming and Boundary Conditions. Transport in Porous Media 11(1): 71–100. DOI: 10.1007/BF00614636.

van Lingen, P., Sengul, M., Daniel, J.-M., and Cosentino, L., 2001. Single medium simulation of reservoirs with conductive faults and fractures. SPE 68165. DOI: 10.2118/68165-MS.

Parisio, F., Vinciguerra, S., Kolditz, O. and Nagel, T., 2019. The brittle-ductile transition in active volcanoes. Scientific Reports 9:143. DOI: 10.1038/s41598-018-36505-x.

Pedroso, C.A. and Correa, A.C.F., 1997. A new model of a pressure-dependent-conductivity hydraulic fracture in a finite reservoir: constant rate production case. SPE 38976.

Pruess, K., Oldenburg, C., Moridis, G., 2012 TOUGH2 User's Guide, Version 2. Earth Sciences Division, Lawrence Berkeley National Laboratory. Report LBNL-43134.

530 Sillitoe, R.H., 2012. Porphyry Copper Systems. Econ. Geol. 105: 3–41. DOI:
531   10.2113/gsecongeo.105.1.3.

532 Streit, J. and Cox, S.F., 2001. Fluid pressures at hypocenters of moderate to large
533   earthquakes. J. Geophys. Res. 106(B2): 2235–2243. DOI: 10.1029/2000JB900359.

534 Vitovtova, V.M., Shmonova, V.M., and Zharikova, A.V., 2014. The porosity trend
535   and pore sizes of the rocks in the continental crust of the earth: evidence from
536   experimental data on permeability. Izvestiya, Physics of the Solid Earth 50(5): 593–
537   602. DOI: 10.1134/S1069351314040181

538 Watanabe, N., Numakura, T., Sakaguchi, K., Saishu, H., Okamoto, A., Ingebritsen,
539   S.E., and Tsuchiya, N., 2017. Potentially exploitable supercritical geothermal re-
540   sources in the ductile crust. Nat. Geosci. 10: 140–144. DOI: 10.1038/NGEO2879.

541 Weis, P., Driesner, T., and Heinrich, C.A.,2012. Porphyry-copper ore shells form at
542   stable pressure-temperature fronts within dynamic fluid plumes. Science 338: 1613–
543   1616. DOI: 10.1126/science.1225009.

544 Weis, P., Driesner, T., Coumou, D., Geiger, S., 2014. Hydrothermal, multi-phase con-
545   vection of H_2O-NaCl fluids from Ambient to magmatic temperatures: a new nu-
546   merical scheme and benchmarks for code comparison. Geofluids 14: 347–371. DOI:
547   10.1111/gfl.12080.

548 Weis, P., 2015. The dynamic interplay between saline fluid flow and rock permeability
549   in magmatic-hydrothermal systems. Geofluids 15: 350–371. DOI: 10.1111/gfl.12100.